Surface Variability Mapping and Roughness Analysis of the Moon Using a Coarse-Graining Decomposition

Siyu Xue¹, Benjamin A. Storer¹, Rachel C. Glade², and Hussein Aluie^{1,3,4}

¹Department of Mechanical Engineering, University of Rochester, Rochester, NY, USA
 ²Department of Earth and Environmental Sciences, University of Rochester, Rochester, NY, USA
 ³Laboratory for Laser Energetics, University of Rochester, Rochester, NY, USA
 ⁴Department of Mathematics, University of Rochester, Rochester, NY, USA

Key Points:

11

13

- Two novel metrics for surface variability display distinct characteristics for highlands, maria, and various geological features.
- Topographic spectra spanning 1 to 5000 km identify four roughness characteristic changes that correlate with known crater distributions.
- Frequencies of fine elevation highlight and contrast scale- and terrain- dependent behaviors between mare and highlands regions.

Corresponding author: Benjamin A. Storer, benjamin.storer@rochester.edu

Abstract

15

16

17

18

19

20

21

22 23

24

25

26

27

28

29

31

32

33

34

35

36

37

39

40

41

42

43

45

47

48

49

51

52

54

55

56

57

61

62

63

The lunar surface contains a wide variety of topographic shapes and features, each with different distributions and scales, and any analysis technique to objectively measure roughness must respect these qualities. Coarse-graining is a naturally scale-dependent filtering technique that preserves scale-dependent symmetries and produces coarse elevation maps that gradually erase the smaller features from the original topography. In this study of the lunar surface, we present two surface variability metrics obtained from coarse-graining lunar topography: fine elevation and coarse curvature. Both metrics are isotropic, deterministic, slope-independent, and coordinate-agnostic. Fine (detrended) elevation is acquired by subtracting the coarse elevation from the original topography and contains features that are smaller than the coarse-graining length-scale. Coarse curvature is the Laplacian of coarsened topography, and naturally quantifies the curvature at any scale and indicates whether a location is elevated or depressed relative to its neighborhood at that scale. We find that highlands and maria have distinct roughness characteristics at all length-scales. Our topographic spectra reveal four scale-breaks that mark characteristic shifts in surface roughness: 100 km, 300 km, 1000 km, and 4000 km. Comparing fine elevation distributions between maria and highlands, we show that maria fine elevation is biased towards smaller-magnitude elevations and that the maria-highland discrepancies are more pronounced at larger length-scales. We also provide local examples of selected regions to demonstrate that these metrics can successfully distinguish geological features of different length-scales.

Plain Language Summary

Planetary surface roughness is inherently scale-dependent: a seemingly smooth surface can look rough if you zoom in enough. The converse can also hold: small-scale rough features can look smooth if you zoom out enough. Therefore, it is important to have a way to measure surface roughness that accounts for variations in how 'zoomed in' we are looking. In this work we use coarse-graining, an approach that effectively blurs the lunar surface, allowing us to vary the 'zoom' level as we are measuring surface variability. We present two ways of measuring the scale-dependent variability of the lunar surface: coarse curvature (measures how curved the blurred surface is) and fine elevation (looks at everything that was removed by the blurring, and measures how much those smaller features contributed to the topography). Using our approach, we are able to incrementally change what is considered 'small' and measure how the perception of the lunar surface changes as we are gradually zooming out of it. Our results highlight the dichotomy in roughness between the lunar maria and highlands. We also identify four key length-scales where the roughness changes qualitatively, suggesting a change in the underlying physical processes that contribute to different kinds of roughness.

1 Introduction

Topographic roughness, which we regard in this work as conveying the extent to which surface elevation varies at different length-scales, is an important measure in geological studies of planetary surfaces. Roughness is necessarily a scale-dependent property: a cue ball, which appears smooth to the touch, has rough surfaces when viewed at sufficiently small scales; and when scaled down to the size of a cue ball, Earth's surface has similar roughness (Anderson & Anderson, 2010). Kreslavsky and Head III (2000) study the kilometer-scale roughness of the Martian surface and conclude that different geological features have distinctive roughness characteristics (e.g. Amazonis Planitia and Vastitas Borealis), and that these characteristics can help with distinguishing the different fundamental processes that produced them. Kreslavsky et al. (2013) calculate the roughness of the lunar surface and propose that hectometer-scale roughness mainly depends on regolith accumulation and recent modification processes, whereas kilometer-

scale roughness corresponds to early geological events. Cai and Fa (2020) discover that lunar surface roughness at meter- to hectometer-scales is dominated by small degraded impact craters. The comparison of roughness at different length-scales can assist in determining the relative geological age of the planetary surface if given sufficient prior knowledge of the surface roughness formation process (Kreslavsky et al., 2013). In addition to gaining geological knowledge, roughness can also be used in geological and geomorphological mapping.

The goals of this study are to (1) present an objective method based on coarse-graining to map the surface variability at different length-scales, (2) map the lunar surface topography across a wide range of length-scales (1 km - 5000 km) using two different metrics, and (3) demonstrate the importance of "length-scale" in mapping the surface roughness. In recent years coarse-graining has proven useful for gaining scale-aware insight into the energetic structures and pathways of Earth's oceans (Rai et al., 2021; Storer et al., 2022; Buzzicotti et al., 2023; Storer et al., 2023; Khatri et al., 2024). Essentially, coarse-graining smooths out the original surface at different length-scales by convolving the elevation data with a scale-dependent normalized kernel. In this study, we use the coarse-graining method to decompose all features on a topographic map to their corresponding length-scales, while maintaining spatial information. This paper is organized as follows. First, it briefly reviews previously published roughness mapping methods and introduces the coarse-graining method. Then the paper presents the scale-dependent surface variability mappings and wavenumber spectra produced by coarse-graining the lunar surface. Lastly, the paper ends with a discussion of the coarse-graining method as well as the results it produces.

2 Previous Roughness Metrics

Mapping roughness to different length-scales enables one to separate small-scale features from the dominant ones so that an equal amount of attention can be given to geological features of all length-scales. Although there is not yet a standard way of mapping topographic roughness at different length-scales nor a standard definition for surface roughness, numerous previous studies provide methods attempting to tackle this problem on the planetary surface (M. W. Smith, 2014). The following is not meant to be an exhaustive list, but a brief outline of the various common methods of measuring roughness.

Statistics Rosenburg et al. (2011) map lunar surface roughness, with scales ranging from 17 m to 2.7 km, using median absolute slope, median differential slope, and Hurst exponents, which describes how slopes scale with length-scale. The authors conclude that the lunar highlands and the mare plains have different roughness characteristics. They also find that most of the lunar surface has fractal-like behavior, with a single or two different Hurst exponents over a scale range. The transition typically occurs near the 1 km scale, implying a significant shift in the surface roughness characteristic, which further indicates two or more competing surface processes. The Hurst exponent has a median value of 0.95 at the lunar highlands, implying that highlands small-scale roughness is similar to large-scale roughness; whereas, in the maria, the median value of the Hurst exponent is 0.76, suggesting that roughness at larger scales is smoother compared to roughness at smaller scales.

Three-point Curvature Kreslavsky et al. (2013) calculate the interquartile range of curvature at several length-scales (115 m, 460 m, 920 m, and 1.8 km) using Lunar Orbiter Laser Altimeter (LOLA) data along each orbital track. The authors approximate the curvature by calculating the second derivative using three data points along the orbit tracks. The distance between the three points is decided by the chosen scales. Then the authors compute the interquartile range of curvatures within a certain proximity of a pixel, and they normalize all pixels' interquartile ranges by a value for typical highlands to obtain topographic roughness maps. Their results show that hectometer-scale

roughness is controlled by processes that happened more recently (1–2 Ga), and kilometerscale roughness is controlled by major geological events that occurred earlier in the history of the Moon, such as basins, volcanism, and tectonic events. Due to different sets of processes and time scales, the roughness maps at the hectometer-scale and the kilometerscale are poorly correlated.

Morphological Method The morphological method from image processing is used by Cao et al. (2015) to build lunar surface roughness maps using LOLA Gridded Data Records (GDRs). The morphological method that controls the scale of the local spatial regions is the structuring element (SE). SEs can have different shapes, and the size is determined by the number of GDR points included. Using SE, the authors smooth the surface down (erosion) and roughen the surface up (dilation). The authors obtained the surface roughness by subtracting the morphological opening and closing, which respectively come from the erosion and dilation. The authors discover a strong roughness contrast between maria and highlands in their global roughness maps.

Local Fractal Dimension Pardo-Igúzquiza and Dowd (2022) use the local fractal dimension to map the surface roughness of the Martian landscape. The roughness at each point is calculated as the local fractal dimension inside moving windows that are within the 41 × 41 pixels region centering the pixel of interest. The fractal dimension of each pixel is estimated using the variogram (Matheron, 1963), a statistical function that describes the dissimilarity between two random variables separated by a certain distance. The authors argue that the variogram method is suitable here because fractional Brownian motion is an appropriate stochastic model for representing natural surfaces. In this study, the authors find that a Martian landscape can have different roughness characteristics at hectometric and kilometric scales.

Wavelet Leaders Method The Wavelet Leaders Method (WLM), a wavelet-based multifractal formalism developed by Jaffard (2004), is used to map the lunar surface roughness at different scale ranges (Deliège et al., 2017; Lemelin et al., 2020). The WLM is an adaptation of the box-counting method in the context of the discrete wavelet transform (Deliège et al., 2017), and it calculates the Hölder exponent which compares theoretical wavelet and topographic values for each pixel (Jaffard, 2004). The WLM allows the identification of scale breaks as well as the identification of scaling regimes. It also indicates if the surface represented by a given pixel tends toward a monofractal or a multifractal behavior within a given scaling regime. In their study, the Hölder exponent quantifies the change of roughness within different scaling regimes — a low exponent value indicates small changes in roughness, and a large value indicates larger changes. Using the WLM, Lemelin et al. (2020) find that the roughness shows distinct characteristics at scale ranges of 330-659 m, 1.3-21.1 km, 42.2-168.8 km, based on the distances measured at the equator. They propose that these characteristic scaling regimes are the results of past major geological events.

3 Methodology

The properties of many geological features, such as the shape's perimeter and line length, change when measured at different scales. Since planetary topography possesses such an intricate nature, a scale-dependent spectrum is an ideal perspective to quantify the surface roughness. Kreslavsky et al. (2013) propose several qualities that constitute a good roughness mapping method: (1) the mapped roughness properly reflects the actual roughness, (2) the tilt of the surface should not change the roughness value, (3) roughness should be scale-dependent, and (4) the mapping of roughness should be stable. The discussion above suggests that a physically informative, robust, and isotropic scale-dependent method is needed when studying surface roughness.

In this study, we propose two metrics—fine elevation and coarse curvature—to map surface variability at different length scales. Additionally, we introduce topographic spectra to identify the length scales at which roughness characteristics change. All these metrics utilize the scale-dependent coarse elevation produced by coarse-graining.

3.1 The Coarse-graining Method

Commutative coarse-graining (Storer & Aluie, 2023) has been recently utilized in calculating the global kinetic energy spectrum of the ocean's surface geostrophic circulation (which is directly tied to sea surface topography) (Storer et al., 2022; Buzzicotti et al., 2023). This was only possible due to recent works that extended and developed commutative coarse-graining applications for the sphere (Aluie, 2019). The first intuition of applying the coarse-graining method for mapping lunar surface roughness originated from the similarity of shapes. The geometrical shapes of many geological features on the lunar surface – craters, basins, and maria, resemble the geometrical shapes of ocean surface circulations. Coarse-graining convolves the original surface elevation data h with a normalized kernel $G_{\ell}(x)$ and can be viewed as a locally-weighted moving average. This process is repeated for every single pixel of interest and at any length-scale of interest. The coarse elevation, \bar{h}_{ℓ} , is produced from coarse-graining h at length-scale ℓ :

$$\overline{h}_{\ell}(x) = G_{\ell}(x) * h(x), \tag{1}$$

where *, in the context of this work, is convolution on the sphere (Aluie, 2019), and x indicates the location on the lunar surface. The convolution process can be intuitively depicted as blurring the elevation within a region centered at x with diameter ℓ . The coarse-graining method employs a low-pass filter that removes features smaller than a given length-scale ℓ , and the obtained coarse topography contains only features with length-scales larger than ℓ .

In this study, the graded top-hat kernel is chosen for $G_{\ell}(x)$ (Storer et al., 2022):

$$G_{\ell}(x) = \frac{1}{A} \left(1 - \tanh\left(10 \left(\frac{\gamma(x)}{\ell/2} - 1\right)\right) \right). \tag{2}$$

In Eq. (2), A is a normalization factor that ensures $G_{\ell}(x)$ can be integrated to unity on the sphere. We use geodesic distance, $\gamma(x)$, to compute the length-scale ℓ between any location x on the Moon's surface and the location where coarse-graining is being performed. Using the geodesic distance preserves the distance between two points on a sphere while working with the Cartesian/lat-lon data. We use the graded top-hat kernel because of its well-defined characteristic length-scale ℓ , but other kernels that have well-defined length-scales can also be used.

Coarse-graining has several qualities that make it a favorable method for mapping planetary surface roughness. First of all, coarse-graining can map the surface variability to different length-scales. Since the kernel used in coarse-graining is determined by the geodesic distance between two locations on the surface rather than the number of grid points between two points, the roughness at the equator and the polar regions will not be discriminated as the result of projecting a sphere onto a rectangular grid. Coarse-graining filters the entire global lunar surface at the same time, removing the need for tapering or detrending that would otherwise be required to apply e.g. Fourier analysis on a smaller region. Additionally, since coarse-graining produces a global map of the filtered fields using only local information, it also allows for regional analysis from the global maps, unlike spherical harmonics, which are unable to produce regional analyses due to the necessarily global nature of the basis functions (Aluie et al., 2018; Buzzicotti et al., 2023). When coarse-graining the elevation data, the outputs are still elevation data, which ensures that the physical meaning of the original data is preserved. Moreover, the coarse-graining method is deterministic, meaning that the resulting coarse elevation would be

the same each time the method is performed. In addition, the coarse-graining method is isotropic; for example, when there is an oval-shaped feature on the surface, the wavenumber spectrum of squared coarse elevation is independent of the direction that oval is pointing.

3.2 Scale-Dependent Metrics of Topography

3.2.1 Coarse Topography and Topographic Spectra

Since a normalized kernel is used, the spatial average of coarse elevation will be conserved across all filtering length-scales (Figure S2) (Aluie, 2019). Therefore, when evaluating how \overline{h}_{ℓ} changes with respect to ℓ , we use the notion of cumulative spectrum \mathcal{E}_{ℓ} :

$$\mathcal{E}_{\ell} = |\overline{h}_{\ell}|^2,\tag{3}$$

Intuitively, the notion of squared elevation is an analogy to the energy of the coarse-grained geostrophic flow at length-scales larger than ℓ . Sadek and Aluie (2018) show, in fluid mechanics, coarse-graining can be used to extract the energy content at different length-scales, and the resulting quantity is called the filtering spectrum, $\overline{E}(k_{\ell})$, where filtering wavenumber $k_{\ell} = 1/\ell$. In the case of coarse-graining lunar topography, the filtering spectrum is obtained by differentiating \mathcal{E}_{ℓ} with respect to k_{ℓ} :

$$\overline{E}(k_{\ell}) = \frac{d}{dk_{\ell}} \{ \mathcal{E}_{\ell} \} = -\ell^2 \frac{d}{d\ell} \{ \mathcal{E}_{\ell} \}, \tag{4}$$

where $\overline{E}(k_{\ell})$ is achievable because of Parseval's theorem. The filtering spectrum is a generalization of the traditional Fourier spectrum, as coarse-graining offers a way to measure energy distributions without relying on a Fourier transform. The filtering spectrum yields the Fourier spectrum with a specific choice of filtering kernel (e.g., the Dirichlet kernel (Rivera et al., 2014)), which is often unsuitable for bounded domains or for spatially local analysis. Sadek and Aluie (2018) determine $\overline{E}(k_{\ell})$ as meaningful by identifying that G_{ℓ} 's scaling agrees with that of the traditional Fourier spectrum (where Fourier analysis is applicable). More discussion about this filtering spectrum can be found in Sadek and Aluie (2018). In the following text, when producing regional or global spectra, we use $\langle \cdots \rangle$ to denote that a spectrum is spatially averaged over regions.

3.2.2 Fine-Scale Elevation

The first metric we use to map the surface variability at length-scale ℓ is the fine elevation $h'_{\ell}(x)$, defined as:

$$h'_{\ell} = h - \overline{h}_{\ell},\tag{5}$$

where h is the elevation model from LOLA GDR. h'_{ℓ} contains features smaller than ℓ due to the linearity of convolution (Aluie, 2019). It is worth noting that some authors use the term "detrended topography" for "fine elevation", and a non-linear analog of fine elevation of the Moon was introduced previously by Kreslavsky et al. (2017), where the detrended elevation of each location is calculated as the difference between its elevation and the median elevation of all pixels within a certain radius (Kreslavsky, 2023). There are also studies that use the variance of detrended topography to quantify the hillslope roughness, which would be equivalent to using $(h'_{\ell})^2$ (Doane et al., 2023, 2021).

How h'_{ℓ} quantifies small-scale variability becomes clear from the identity (Eyink, 2005; Aluie, 2017),

$$h'_{\ell}(\mathbf{x}) = h(\mathbf{x}) - \overline{h}_{\ell}(\mathbf{x}) = -\int d^2 \mathbf{r} G_{\ell}(-\mathbf{r}) \left[h(\mathbf{x} + \mathbf{r}) - h(\mathbf{x}) \right], \tag{6}$$

in a two-dimensional flat space. Recall that the kernel $G_{\ell}(-\mathbf{r})$ in Eq. (2) is symmetric, such that $G_{\ell}(-\mathbf{r}) = G_{\ell}(\mathbf{r})$, and it is approximately a Top-hat function with values 1

within $|\mathbf{r}| < \ell/2$ and zero for larger $|\mathbf{r}|$. Therefore, the right-most term of Eq. (6) shows that $h'_{\ell}(\mathbf{x})$ is a spatial average of the increment $[h(\mathbf{x}+\mathbf{r})-h(\mathbf{x})]$ within a circular region, which is centered at \mathbf{x} with a diameter ℓ (Aluie et al., 2022). Increments such as $h(\mathbf{x}+\mathbf{r})-h(\mathbf{x})$ in Eq. (6) are well-known in the mathematics literature (e.g., the subject of functional analysis) to quantify the differentiability of a function as the separation distance \mathbf{r} is varied (Strichartz, 2003; Evans, 2010; Sogge, 2017; Krantz, 2019; Zhao & Aluie, 2023).

In terms of interpreting the sign of h'_{ℓ} , if the actual surface is higher (lower) than the coarse elevation, h'_{ℓ} would be positive (negative), indicating the small scale feature is above the surface, a "protrusion" ("indentation"). When there is a tilt on the surface, the coarse-graining method will treat the tilt as a very large feature, and since the surface tilt is larger than the filtering length-scale ℓ and h'_{ℓ} contains no information larger than ℓ , surface tilt will not affect h'_{ℓ} , satisfying Kreslavsky's second requirement for roughness metrics.

3.2.3 Large-scale Topographic Curvature

Coarse curvature, $\nabla^2 \overline{h}_{\ell}$, is the Laplacian of the coarse elevation, \overline{h}_{ℓ} , in spherical coordinates:

$$\nabla^2 \overline{h}_{\ell} = \frac{1}{R^2} \left[\tan(\theta) \frac{\partial}{\partial \theta} + \frac{\partial^2}{\partial \theta^2} + \sec^2(\theta) \frac{\partial^2}{\partial \phi^2} \right] \overline{h}_{\ell}, \tag{7}$$

where R is the radius of the Moon, θ is latitude, and ϕ is longitude. The Laplace operator is the divergence of the gradient, and the Laplacian represents the local curvature of a multivariable function. A previous study by Grieve et al. (2016) concludes that the length-scale can affect the measurement of curvature for different geological features. By applying the Laplacian operator to the coarse elevation, we obtain scale-dependent coarse curvature that describes surface roughness. Coarse curvature is chosen for four reasons: (1) different from a first-order derivative, the Laplacian is independent of the slope, (2) the Laplacian has the physical meaning as curvature, (3) when computed in spherical coordinates, the Laplacian has no latitude bias (vs. computing on pixel/Cartesian coordinates), same as h'_{ℓ} , and (4) as the length-scale increases, small features disappear from the coarse curvature, obeying the intuition of scale-dependency.

The Laplacian indicates deviation from the local average, and the "local" here means that the curvature represents properties within a very small domain. It is worth noting that although the deviation is only reflected within a small domain, what goes into that small domain is implicitly controlled by the filtering length-scale. While the magnitude of the Laplacian quantifies the extent of curvature, the sign of the Laplacian indicates whether a point is curving upward or downward within the small domain. More details on interpreting the Laplacian of a 2D scalar function can be found at Figure S1 in the Supplemental Material.

3.2.4 Illustration of Topographic Metrics

Figure 1 shows a lunar equator segment being coarse-grained at selected length-scales. As the filtering length-scale increases, the coarse segment becomes smoother and ignores features smaller than the filtering length-scale [1(a)]. Correspondingly, the fine elevation adopts features with larger and larger length-scales, which overpowers the features of smaller length-scales [1(b)]. It is worth noting that since coarse-graining is scale-dependent, a location can have both positive and negative fine elevation, depending on the filtering length-scale. For example, the central peak boxed in the top panel is not distinctive at $\ell = 1$ km but has positive h'_{ℓ} between $\ell = 5$ km and $\ell = 10$ km. At $\ell = 20$ km and larger, the location at the central peak shows negative h'_{ℓ} . This pattern also explains why the coarse-graining method considers the crater floor to be a larger feature

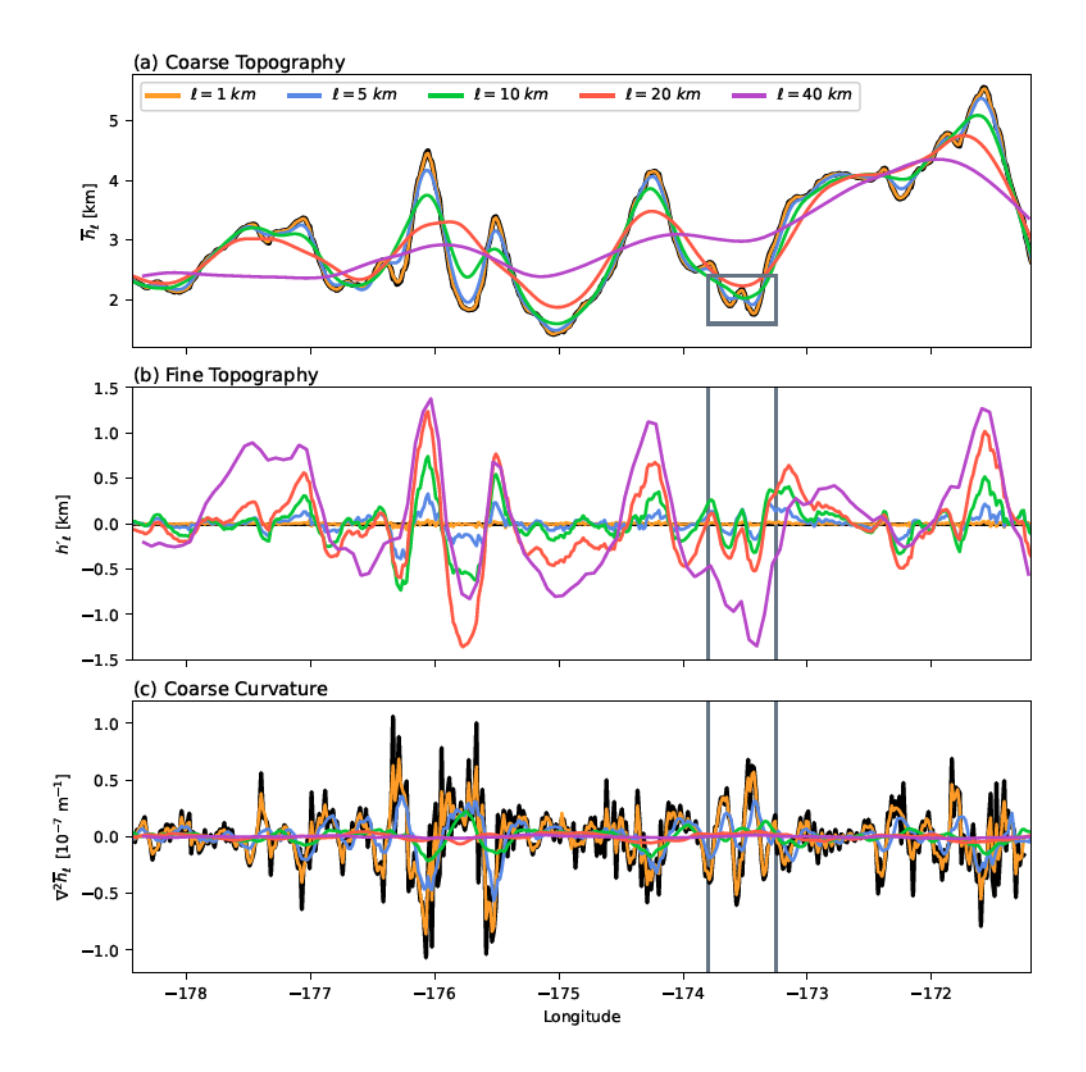


Figure 1. Demonstration of Metrics A slice at the Moon's equator is selected to demonstrate the coarse-graining method. In (a), the black curve (mostly overlaps with $\ell=1$ km) marks the original elevation, h, and the colored curves indicate the coarse elevation, \overline{h}_{ℓ} . (b) plots the fine elevation, h'_{ℓ} , at the corresponding length-scale ℓ . In (c), the black curve marks the 1D original curvature, and the colored curves plot the 1D coarse curvature, $\nabla^2 \overline{h}_{\ell}$. For better visualization, the plotted original and 1 km curvature (black and orange lines) were smoothed with a five-point moving average. One degree at the lunar equator is approximately equivalent to 30 km.

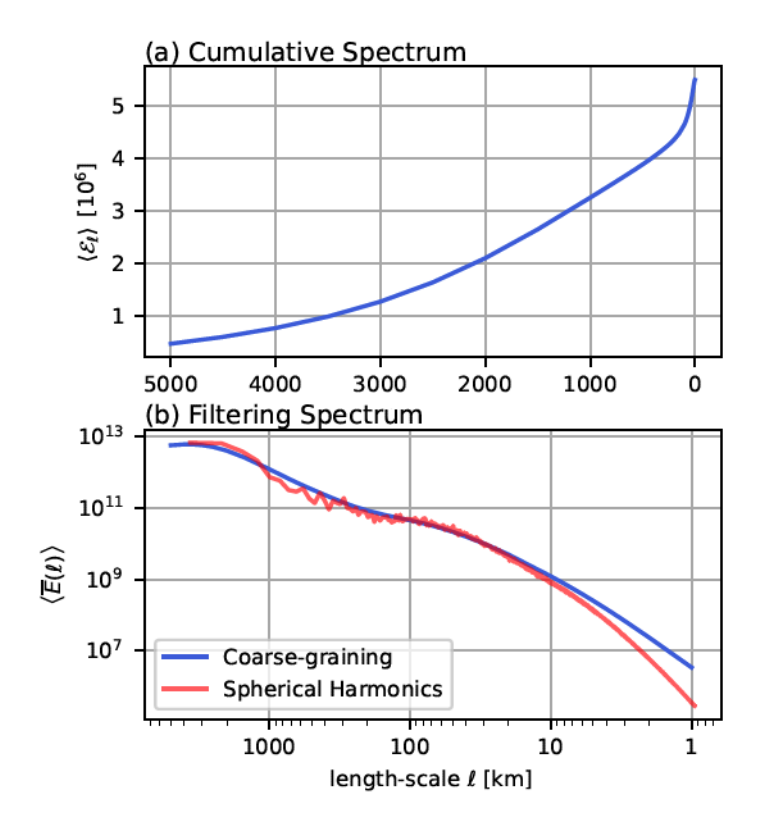


Figure 2. Topographic Spectra (a) the spatially averaged cumulative spectrum $\langle \mathcal{E}_{\ell} \rangle$ (Eq. 3) and (b) the spatially averaged filtering spectrum $\langle \overline{E}(k_{\ell}) \rangle$ (Eq. 4), as a function of ℓ , is compared with the filtering spectrum from spherical harmonics (Wieczorek, 2024). Note that the two panels use different horizontal axes.

compared to the crater rim in Figure 4 and 10 — the rim has a large diameter, but itself is rather narrow.

Similar to the coarse elevation, as the filtering length-scale increases, the coarse curvature gradually approaches zero, ignoring features smaller than the filtering length-scale [1(c)]. For example, the two small troughs boxed in the top panel have large curvature magnitudes, and as ℓ increases, the corresponding curvature magnitudes decrease. At $\ell=10$ km, the coarse curvature omits these two small troughs and approaches zero. Similar to the gradient, which emphasizes small-scale features, the Laplacian is also sensitive to small-scale features. This explains why the original curvature and $\nabla^2 \overline{h}_{\ell=1km}$ segments have more fluctuations. In the coarse curvature panel, the two troughs have positive curvature since all their surrounding points have higher elevations, and the peak has negative curvature since it is higher than its surrounding points.

The cumulative spectrum of the entire lunar surface, computed using Eq. 3, and its corresponding filtering spectrum, computed using Eq. 4, are plotted in Figure 2. The cumulative spectrum of the entire lunar surface $\langle \mathcal{E}_{\ell} \rangle$ decreases as the filtering length-scale increases [2(a)], and Jensen's inequality guarantees that it is a monotonic decrease (Sadek & Aluie, 2018). This decrease corresponds to an overall smoothing of the surface. The filtering spectrum of the entire lunar surface $\langle \overline{E}(k_{\ell}) \rangle$ is plotted in Figure 2(b). Filtering spectra from coarse-graining and from spherical harmonics show general agreement, with the spherical harmonics one being slightly steeper at smaller length-scales ($\ell < 10km$). It has been shown (Sadek & Aluie, 2018) that when using a 1st-order kernel such as the

one adopted in our work, filtering spectra cannot decay faster than k^{-3} and higher order kernels are needed to detect steeper spectra.

The slope of the log-log $\overline{E}(k_{\ell})$ curve is related to the change in \mathcal{E}_{ℓ} when moving from a larger length-scale to a smaller length-scale. A change in the spectral slope implies something special happens to \overline{h}_{ℓ} at the corresponding length-scales, at which the surface roughness characteristics have changed; for example, the length-scale corresponding to a flatter slope is more dominant. With such qualities, the spectral slope (Figure 7) can help with identifying scale breaks of the Moon's surface roughness. Moreover, it is generally appreciated in the turbulence literature that spectral slopes reflect the smoothness of a field (see Fig. 1 in (Aluie, 2017) and the associated discussion), with steeper spectral scaling implying smoother (or, broadly, less turbulent) fields (Aluie et al., 2022). The slopes of spectra can also help identify what type of noise signal is present.

3.3 Data

325

326

327

328

329

330

331

332

334

335

336

337

339

340

341

342

343

344

345

346

348

349

352

353

354

357

358

350

360

361

362

366

367

369

370

This study uses the global elevation model from LOLA GDR, downloaded from the NASA Planetary Data System (Neumann, 2010). The models with resolution of 4 pixels per degree, 16 pixels per degree, and 64 pixels per degree (approximately 7.6 km, 1.9 km, and 0.5 km equatorial grid-spacing respectively) are selected to map the global topographic roughness of the lunar surface. Utilizing higher-resolution topographies (128 pixels per degree and 256 pixels per degree) is possible but is computationally expensive for global topographic roughness.

LOLA is an altimeter on the payload of NASA's Lunar Reconnaissance Orbiter space-craft (D. E. Smith et al., 2010) and is designed to precisely measure the distance from the spacecraft to the lunar surface and incorporate precision orbit determination. LOLA has 5 beams and operates at 28 Hz, with a nominal accuracy of 10 cm (D. E. Smith et al., 2010). The LOLA GDR is a gridded dataset that includes the elevation model of the lunar surface, obtained from binning and averaging the calibrated measurements from LOLA. We confirm that in this LOLA data, the elevation is relative to a geoid and has an area average of $\mathcal{O}(10^{-6})$, and so our cumulative spectra are objective.

3.4 Data Downsampling to Filter at Very Large Scales

Applying coarse-graining to the entire sphere can be computationally expensive, especially when the data resolution is high and the filtering length-scales are large. To save computation time, it is wise to use data with lower resolutions when filtering at larger length-scales. Since coarse-graining is a deterministic method, when using data with different resolutions, the filtered result of the lower resolution is a compressed version of that of the higher resolution. Figure S2 in the Supplemental Material shows that when using elevation data at different resolutions, the spatial average of \mathcal{E}_{ℓ} converges, as seen in the overlapping curves. The slight differences between curves are insignificant and can be attributed to numerical errors. The coarse curvatures of all three resolutions are less aligned at their corresponding smaller length-scales. These discrepancies are the result of computing the gradient without sufficient sampling. We avoid this potential numerical error by using finer resolution for smaller length-scales: 64 pixels per degree resolution for $\ell = 1 - 20$ km, 16 pixels per degree for $\ell = 30 - 100$ km, and 4 pixels per degree resolution for $\ell > 100$ km. It is worth noting that since the Laplacian is sensitive to small-scale features, and topography with higher resolution contains more details, the coarse curvature at the polar regions is prone to have higher curvature magnitudes due to finer data sampling.

3.5 Comparison with Previous Methods

The above qualities of the coarse-graining-based methods can complement many previous roughness mapping methods. Median absolute slope, median differential slope, and Hurst exponent, used by Rosenburg et al. (2011) are statistical methods that only reflect certain statistical patterns of roughness. In addition, the Hurst exponent is an estimated slope from line-fitting, and the line-filtering is segmented to multiple ranges by breakover points (Shepard et al., 2001). The three-point curvature (Kreslavsky et al., 2013) samples the surface too sparsely compared to a smooth kernel. The morphological method (Cao et al., 2015) uses is limited to small length-scales because a fixed grid size is susceptible to potential projection distortion at large length-scales. The local fractal dimension method in Pardo-Igúzquiza and Dowd (2022) uses a fixed window size, thus the result is not a purely scale-dependent roughness. The Hölder exponent is computed using WLM with the third-order Daubechies wavelet (Lemelin et al., 2020), and since the third-order Daubechies wavelet is not symmetric, the resulting Hölder exponent values can potentially have a directional component. In addition, Hölder exponents only provide a general estimate of surface roughness rather than a precise pixel-to-pixel roughness value, and it is also susceptible to the distortion of spherical coordinates at large length-scales.

R-Plots R-plots, a common tool for quantifying crater distributions, can be loosely viewed as the proportion of the surface area covered by craters of various sizes (Robbins et al., 2018). It is important to recognize that while R-plots and the spectra presented here are related, direct comparisons are non-trivial, and may be confounded by characteristics other than crater area. This is because the filtering spectra do not only measure craters, but all geological features (e.g. rills/rimae), and further do not only measure the area of the features, but also their intensity (e.g. doubling the depth of craters while preserving their area would modify their spectral signal but not the R-plot). While a peak in the R-plot may indicate a peak at the corresponding scale in the spectrum from the increased frequency of features at the given scale, it is neither a necessary nor sufficient condition. The presence of a peak in one that is absent in the other may provide insight into the quality of the features (e.g. a peak in the spectrum that is absent in the R-plot may indicate non-crater features at that scale).

4 Results

371

372

373

374

375

376

377

381

382

383

384

388

389

390

391

392

393

397

400

401

405

406

407

408

411

412

413

414

415

416

417

418

419

420

By coarse-graining the entire lunar surface at different length-scales, surface variability at each length-scale can be disentangled. Figure 3 shows the coarse elevation corresponding to $\ell=10$ km, 50 km, 100 km, and 300 km. The coarse elevation contains all features with length-scales greater or equal to the filtering length-scale. It is worth noting that since the top-hat kernel used in coarse-graining is not sharp-spectral (that is, the Fourier transform of the kernel has energy at all scales, just much less energy at scales smaller than the filter size), the feature length-scales in the coarse elevation are not clean-cut. However, features smaller than the filtering length-scales are preferentially removed. Many small craters in $\overline{h}_{\ell=10km}$ [3(a)] are absent in $\overline{h}_{\ell=50km}$ [3(b)], while $\overline{h}_{\ell=100km}$ [3(c)] features mainly large craters and many basins. At $\ell=100$ km, the concentric features of Mare Orientale are still distinguishable due to its large diameter. $\overline{h}_{\ell=300km}$ [3(d)] highlights the overall geology of the lunar surface – the highlands and the maria. In addition to the simple contrast of high and low lands, the basins are still visible but lost all the inner details and clear boundaries.

4.1 Fine Elevation

Figure 4 shows the fine elevation at $\ell=10$ km, 50 km, 100 km, and 300 km. $h'_{\ell=10km}$ [4(a)] represents small-scale surface features that are almost uniform in the highlands and very sparse in the maria. At $\ell=10$ km, the roughness only distinguishes itself be-

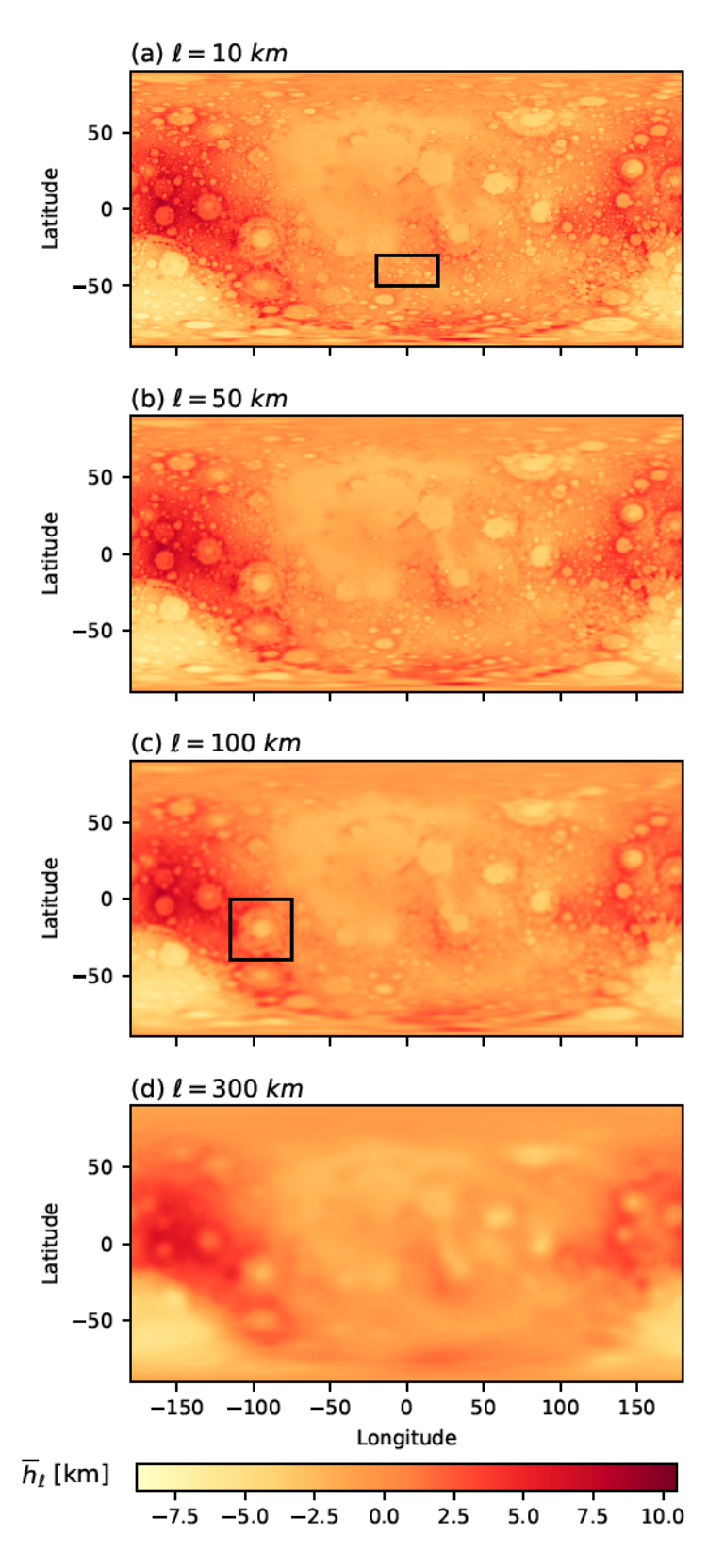


Figure 3. Maps of Coarse Elevation \overline{h}_{ℓ} plotted for (a) $\ell=10$ km, (b) $\ell=50$ km, (c) $\ell=100$ km, and (d) $\ell=300$ km. The box in (a) marks an example of some small craters. The box in (c) marks the location of the Mare Orientale.

tween maria and highlands without involving clear crater figures. In $h'_{\ell=50km}$ [4(b)], the edges of small craters are visible. Some unique details within the maria and basins start to appear, such as inside the Mare Orientale. In $h'_{\ell=100km}$ [4(c)], the raised rims of craters and some basins are marked as positive roughness, embodied in the red circles. The concentric features of the Mare Orientale are well-mapped. In $h'_{\ell=300km}$ [4(d)], the raised rims of all craters and basins are marked with red circles, indicating a protrusion from the surface. The floor of craters and some basins are filled with negative fine elevation, indicating an indentation in the surface. These negative floors are not prevalent in the small length-scale fine elevation maps because the crater floor is a larger-scale feature compared to the crater rim.

In Figure 5, we use the South Pole–Aitken basin as an example to demonstrate that the coarse-graining method can separate small length-scale features from the original topography, and the length-scale is consistent even in the Polar region. The large indentation of the South Pole–Aitken basin due to impact is eliminated in $h'_{\ell=300km}$ [5(b)]. As a result, the rim details of the basin as well as the smaller craters inside the basin are emphasized. It is worth noting again that since the coarse-graining method uses the geodesic distance, the h'_{ℓ} at the polar regions would have the same meaning as the ones at the low-latitude regions.

4.2 Coarse Curvature

Figure 6 plots the coarse curvature at $\ell=10$ km, 50 km, 100 km, and 300 km. At each filtering length-scale, the coarse curvature emphasizes the change of the surface, making it an ideal tool to detect crater rims or other small-scale features. Since the coarse elevation contains only features larger than the filtering length-scale, the coarse curvature keeps omitting small-scale surface changes when the filtering length-scale increases. $\nabla^2 \overline{h}_{\ell=10km}$ [6(a)] highlights how the highlands are densely covered by small craters while the maria are substantially smoother. In $\nabla^2 \overline{h}_{\ell=50km}$ [6(b)], small craters are removed, and the surface is dominated by large craters and lunar basins. In $\nabla^2 \overline{h}_{\ell=300km}$ [6(d)], the boundary of the South Pole–Aitken basin is roughly marked by positive curvature. As the length-scale increases, concentrated high curvature regions would appear in some crater centers. These high curvature regions are the results of flattening the raised rim, causing the adjacent crater floor to elevate and leaving the crater center being the lowest part. In addition to crater centers, the curvature magnitudes are also higher in the polar regions, for the reason discussed in subsection 3.4.

4.3 Wavenumber Filtering Spectra and Scale Breaks

The log-log slope of $\langle \overline{E}(k_{\ell}) \rangle$ curve can help with identifying scale breaks of the Moon's surface roughness (Figure 7). A scale break is the length-scale, at which the characteristics of the surface roughness change. Overall, the total spectral slope is almost identical to the spectral slope of the highlands while significantly different from the spectral slope of the maria. This implies that the roughness characteristics of the lunar surface are dominated by the highlands.

Based on the slopes, we identify four important scale breaks: 100 km, 300 km, 1000 km, and 4000 km. We also identify 1.5 km to be interesting since the mare slope and the high-land slope cross at this length-scale. However, more fine elevation measurements at length-scales smaller than 1 km are needed to ensure 1.5 km is a scale break rather than a numerical artifact when computing the derivative.

These scale breaks can be explained by the total crater area (provided in Robbins (2019)), that is the area of all craters with a specific diameter (length-scale). The total crater area has a wide peak that is centered near $\ell=100$ km, a narrower peak near $\ell=1000$ km, and a spike at the largest length-scale, accounting for the South Pole–Aitken

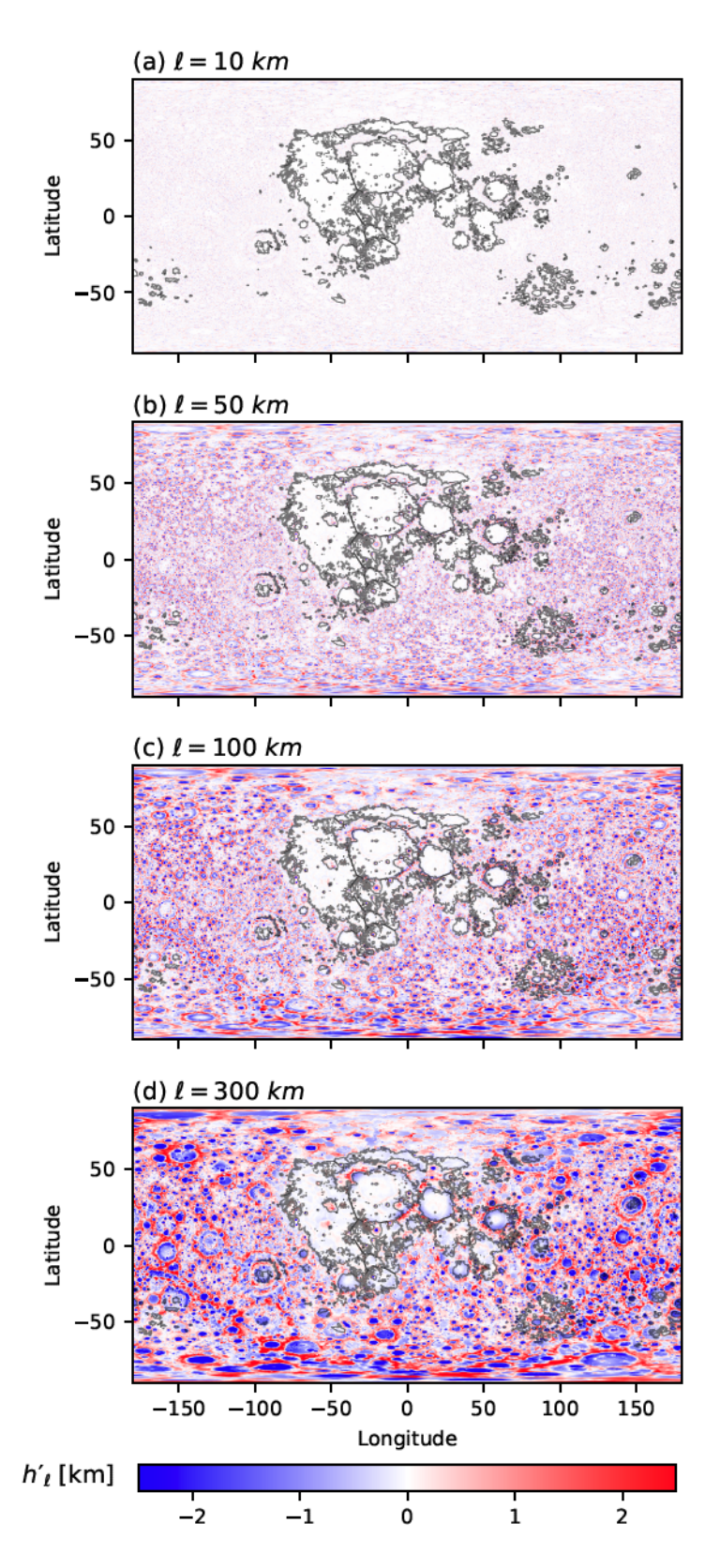


Figure 4. Maps of Fine Elevation h'_{ℓ} plotted for (a) $\ell=10$ km, (b) $\ell=50$ km, (c) $\ell=100$ km, and (d) $\ell=300$ km. The black lines mark the lunar mare boundaries produced by Nelson et al. (2014).

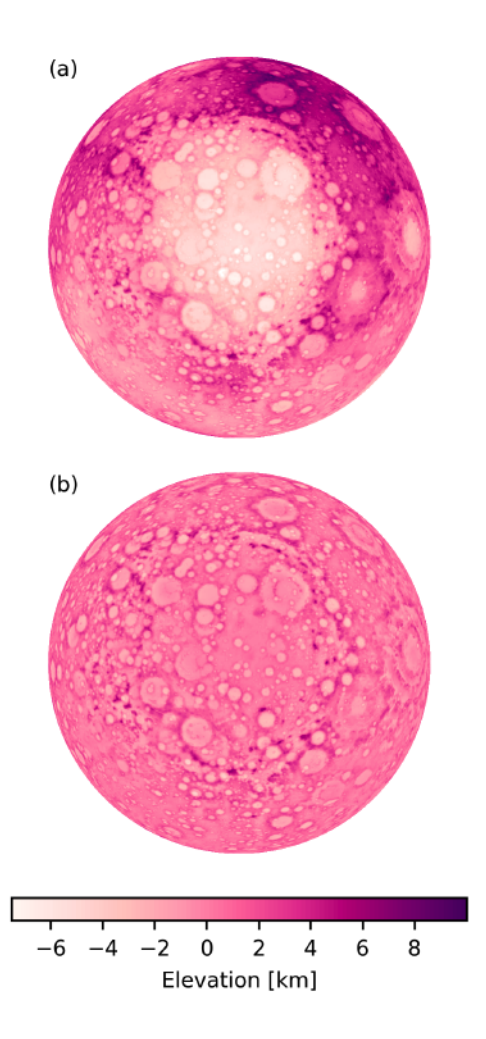


Figure 5. South Pole–Aitken Basin (a) the original elevation map, h and (b) the fine elevation, h'_{ℓ} , at $\ell = 300$ km. View from the South Pole.

470

471

472

473

474

477

478

479

481

482

485

486

487

basin. Both highland and mare slopes reach a plateau near $\ell = 100$ km, matching the total area of large craters. The more negative mare slope near $\ell=100$ km length-scale indicates that the maria have fewer large craters compared to the highlands. In the range of $\ell = 300-1000$ km, the mare slope presents a narrower peak that matches the total crater area curve. The 300-1000 km range includes the lunar basins that essentially constitute the maria; thus, the mare slope crosses the highland slope at $\ell = 300$ km and becomes less negative. Since the basins are absent in the highlands, the highland slope shows no correlation with this range. The total spectral slope crosses zero and becomes positive at $\ell = 3700$ km, slightly shorter than 4000 km, and the slope starts to decrease at $\ell = 4500$ km, slightly larger than 4000 km. This 4000 km scale break can be explained by the huge cluster of lunar maria at the center of Figure 8. If treating the center cluster of lunar maria as a single feature, it would have a length-scale range of 3000-4000 km. At large length-scales near 4000 km, which is almost half of the Moon's circumference, the flattening of total and highland spectra reflects the compactness of the lunar surface as a sphere. We truncate the mare spectrum and slope at $\ell = 1000$ km due to its lack of physical significance and to prevent the mare filtering spectrum from being unduly influenced by coarse-graining edge effects, which can cause highlands surface information to leak into the maria regions.

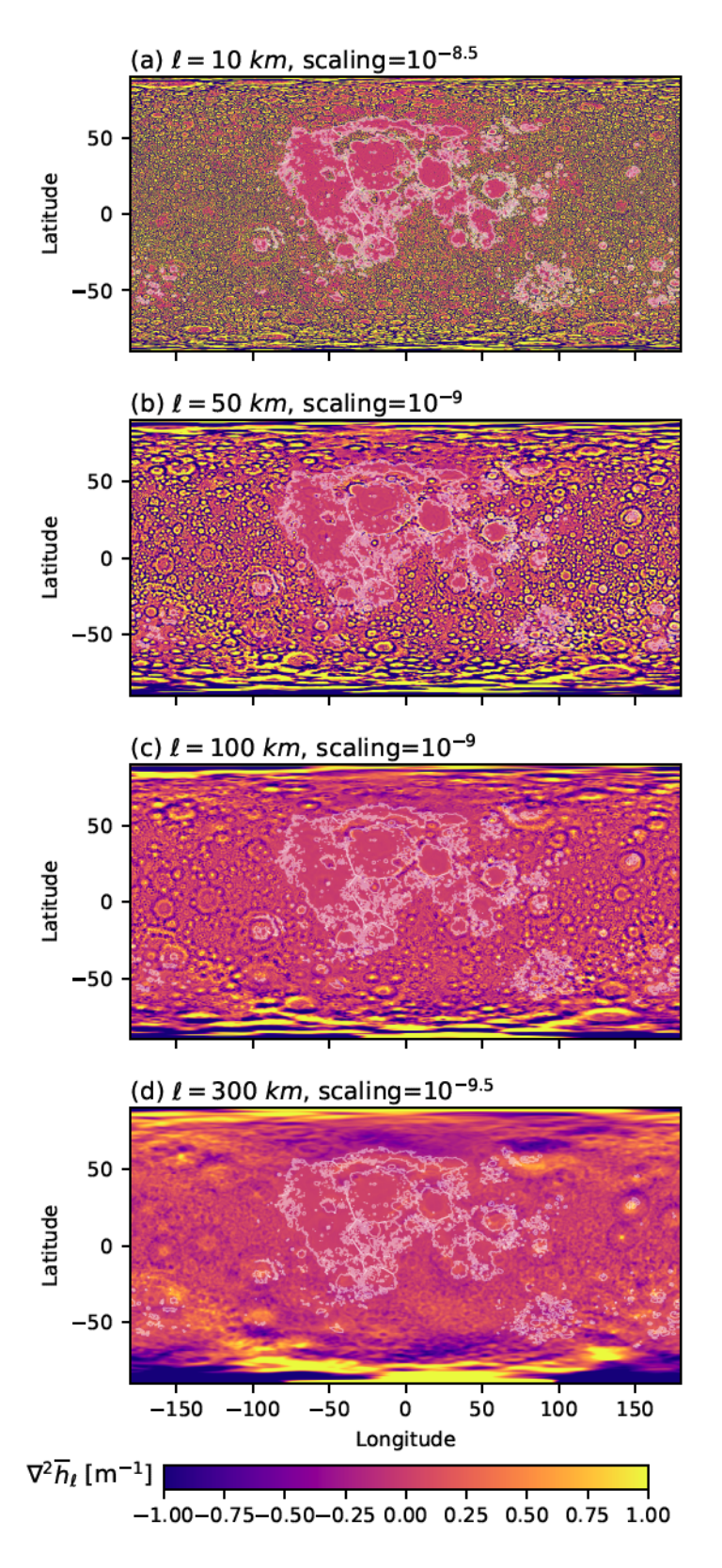


Figure 6. Maps of Coarse Curvature $\nabla^2 \overline{h}_{\ell}$ plotted for (a) $\ell=10$ km, (b) $\ell=50$ km, (c) $\ell=100$ km, and (d) $\ell=300$ km. The white lines mark the lunar mare boundaries produced by Nelson et al. (2014). Each panel is normalized to share a common colorbar, with the scaling factors provided in each panel label.

489

492

493

494

501

502

503

508

509

Although the South Pole–Aitken basin has the largest surface area, its diameter does not match any of the identified scale breaks (as shown in Figure 7). This mismatch can be attributed to basins not having a perfect circular shape. If basins do not have perfect circular shapes, the coarse-graining method considers the basin to have a range of length-scales instead of a single length-scale, and the importance of a single length-scale is debilitated. Therefore, the South Pole–Aitken basin contributes to the increase of the highland slope in the range of $\ell=2000-3000$ km instead of at a mere single value like $\ell=2500$ km. In addition, the general shape of the far side highland, which has similar length-scales as the South Pole–Aitken basin, could also contribute to the range of $\ell=2000-3000$ km (Garrick-Bethell et al., 2010). Similarly, the slopes not reflecting the two small peaks on the total crater area curve between 100 km and 1000 km could be attributed to the same reason. On the other hand, the effect of non-circular shape on the wavenumber spectrum is less pronounced for smaller craters due to their small length-scales – if the actual range of length-scale is within 20% of the fitted diameter, then the smaller crater would have a narrower range.

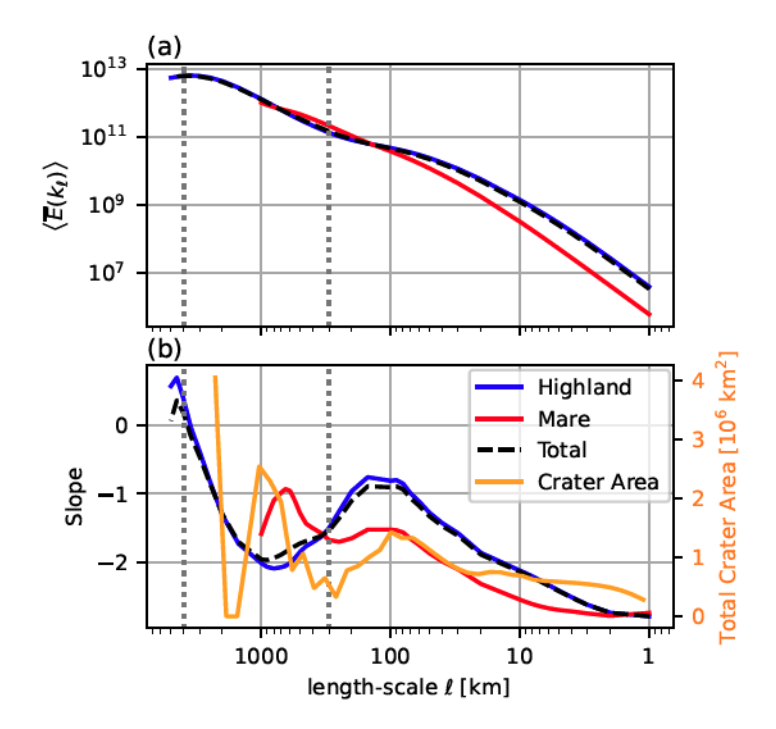


Figure 7. Regional Topographic Spectra (a) $\langle \overline{E}(k_{\ell}) \rangle$ correspond to the maria (red), highlands (blue), and the entire lunar surface (dashed black). (b) spectral slopes of the three $\langle \overline{E}(k_{\ell}) \rangle$ in (a) as well as the sum of all circular areas of craters whose diameter is ℓ . The crater diameters are the circle fit results produced by Robbins (2019). The dotted vertical lines mark $\ell = 300$ km and 4000 km. We use in total 42 different length-scales to construct the spectrum.

4.4 Highland h'_{ℓ} v.s. Mare h'_{ℓ}

We selected ten 5×5 degree boxes in the highland region and ten 5×5 degree boxes in the mare region (locations marked in Figure 8) as sampled locations to compare distributions of fine elevation for highlands v.s maria. For a fair comparison, all boxes are centered on the equator to ensure a consistent surface area. Figure 9 (a) plots the frequency of having a particular fine elevation value within the region at a selected length-scale. It is worth noting that the distribution of mare h'_{ℓ} at $\ell = 30$ km and $\ell = 100$ km

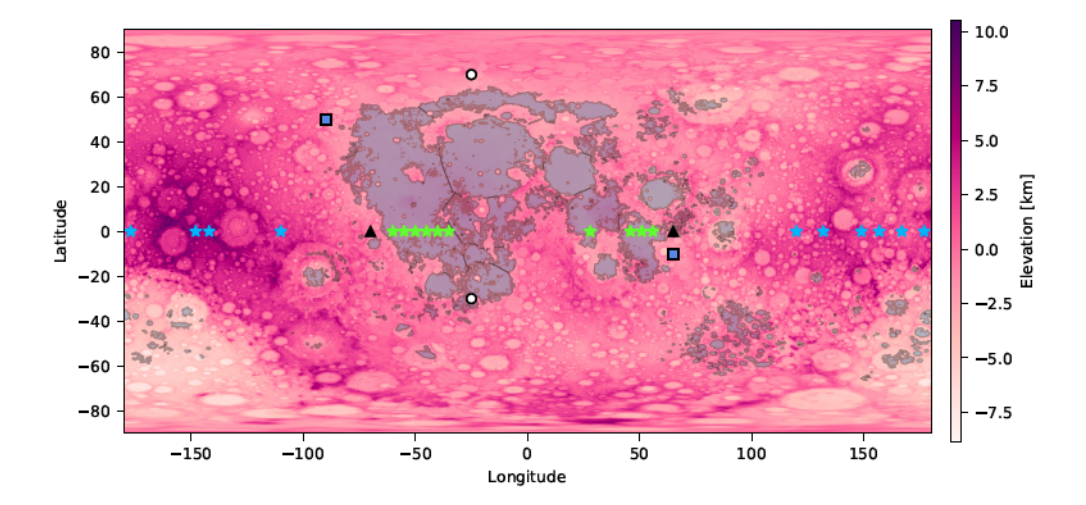


Figure 8. The blue stars mark the centers of the $5^{\circ} \times 5^{\circ}$ boxes sampled in the highland region, and the green starts mark the centers of the $5^{\circ} \times 5^{\circ}$ boxes sampled in the mare region. The grayed areas indicate lunar maria, produced by (Nelson et al., 2014). To illustrate the scale of lunar maria, the geodesic distance is 3032 km between the two white dots, 4093 km between the two black triangles, and 3591 km between the two blue squares.

are almost identical. This implies that most of the geological features within the selected mare regions have length-scales smaller than 30 km. At $\ell=1$ km, 5 km, 30 km, and 100 km, the selected mare regions have narrower frequency curves and higher frequencies near h'=0, which indicates that they are smoother than the selected highland regions at these length-scales. In addition, at each length-scale, having frequency curves with smaller spreads indicates that the range of h'_{ℓ} at the selected mare region is smaller than that of the selected highland region. The above two discrepancies between highland and mare regions are more pronounced at larger length-scale. The spectral slopes of the highland and mare regions [7(b)] deliver the same message that the filtering spectrum of the highland region grows faster as the length-scale increases. In addition, both selected highland and mare regions tend to have more positive h'_{ℓ} than negative h'_{ℓ} ; this implies that more roughness features are "protrusion".

4.5 Local Roughness Maps of Selected Geological Features

Korolev basin The fine elevation and coarse curvature of the Korolev basin at $\ell = 1$ km, 10 km, and 50 km are shown in Figure 10. $h'_{\ell=1km}$ [10(c)] does not show the Korolev basin boundary clearly and only displays small-scale roughness features that are almost uniformly distributed throughout the region. This pattern is not directly visible in the original elevation map. The inside of the Korolev basin and adjacent craters have lower h'_{ℓ} , thus they are slightly smoother than their surrounding terrain. The crater rims are slightly rougher than all other areas. Some of the crater rims have positive h'_{ℓ} on one side and negative h'_{ℓ} on the other side, indicating that one side of the rim is slightly higher out of the surface than the other side. In $\nabla^2 \overline{h}_{\ell=1km}$ [10(d)], the rims of small craters and some crater peaks are marked by negative curvature. The outside of the Korolev basin is more densely covered by small craters compared to its inside. At $\ell = 10$ km [10(e)], the positive rim and negative floor of craters start to appear in h'_{ℓ} . The crater peaks are also marked by positive h'_{ℓ} , for example, Korolev C crater and Korolev M crater. At this length-scale, the roughness difference between the inside and outside of the Korolev basin is more pronounced, with the inside of the basin being smoother; however, the bound-

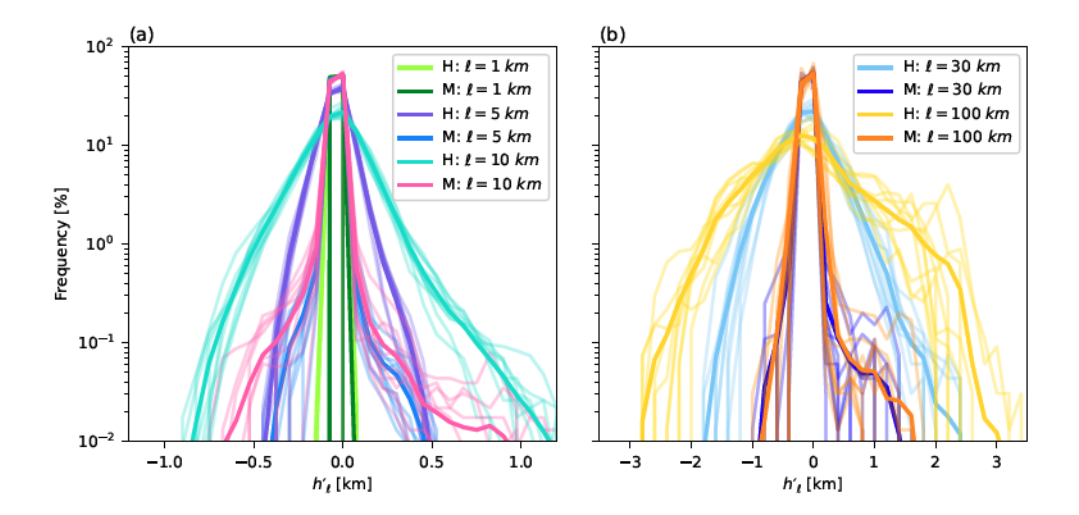


Figure 9. Fine Elevation Distributions The distributions of h'_{ℓ} in selected highland (H) and mare (M) regions (a) at length-scales $\ell=1$ km, $\ell=5$ km, $\ell=10$ km, and $\ell=100$ km; (b) at length-scales $\ell=30$ km and $\ell=100$ km. The locations of the sampled highland and mare regions are marked in Figure 8. Thick lines indicate the average across all samples, while thin transparent lines denote individual samples.

ary of the Korolev basin is still unclear. $\nabla^2 \overline{h}_{\ell=10km}$ [10(f)] highlights the larger craters, and compared to smaller craters, these larger craters are more uniformly distributed inside or outside the basin. As the length-scale increases, the curvature is computed at a larger domain; therefore, most crater floors are filled with negative curvature because the crater floor seen as a whole is lower than its surrounding terrains. In $h'_{\ell=50km}$ [10(g)], the basin rim is visible, and the details on some smaller craters are omitted, as smaller features are overpowered by the larger features. When the filtering length-scale increases, the positive dots that represent crater peaks eventually disappear, for the reason discussed in Figure 1. In $\nabla^2 \overline{h}_{\ell=50km}$ [10(h)], details of craters are absent and the boundary of the Korolev basin is pronounced. The basin rim is marked by negative curvature, and the basin floor adjacent to the rim is marked by positive curvature. $\nabla^2 \overline{h}_{\ell=50km}$ also exhibits several high curvature crater centers, as discussed in Figure 6.

541

545

546

548

550

551

552

553

557

558

565

566

Montes Caucasus Figure 11 shows the fine elevation of Montes Caucasus at $\ell =$ 1 km, 5 km, and 20 km. At $\ell = 1$ km [11(b)], the surface of Montes Caucasus has similar roughness characteristics as the terrain outside of the adjacent maria. At $\ell=5~\mathrm{km}$ [11(c)], the ridges of Montes Caucasus are more pronounced, as characterized by greater positive and negative h'_{ℓ} . The map of $h'_{\ell=20km}$ [11(d)] resembles the general topography of Montes Caucasus. The positive h' indicates hill-like features while the negative h'_{ℓ} indicates valley-like features. At $\ell = 1$ km and 5 km, the ray-like impact ejecta of Aristillus crater (lower left corner) is visible. The wrinkle ridges inside Mare Serenitatis (lower right corner) are visible in $h'_{\ell=5km}$ and $h'_{\ell=20km}$, while absent in $h'_{\ell=1km}$. At $\ell=20$ km, the roughness of the wrinkle ridges is higher on the eastern side. The crater peak of Eudoxus (top right) is highlighted at $\ell = 1$ km and 5 km. It is worth noting that Eudoxus crater peak has both positive and negative h'_{ℓ} because the peak consists of a group of small hills instead of a single peak. Calippus crater floor (near the highest part of Montes Caucasus) has similar h'_{ℓ} as the surrounding Montes Caucasus terrain at $\ell = 1$ km and 5 km, unlike Eudoxus or Cassini. The floor of Cassini crater (west of Montes Caucasus) is flooded, as it has similar roughness characteristics as the surrounding mare. Inside Cassini crater, there is a hilly ridge area in the eastern part, and the hilly ridge feature is vis-

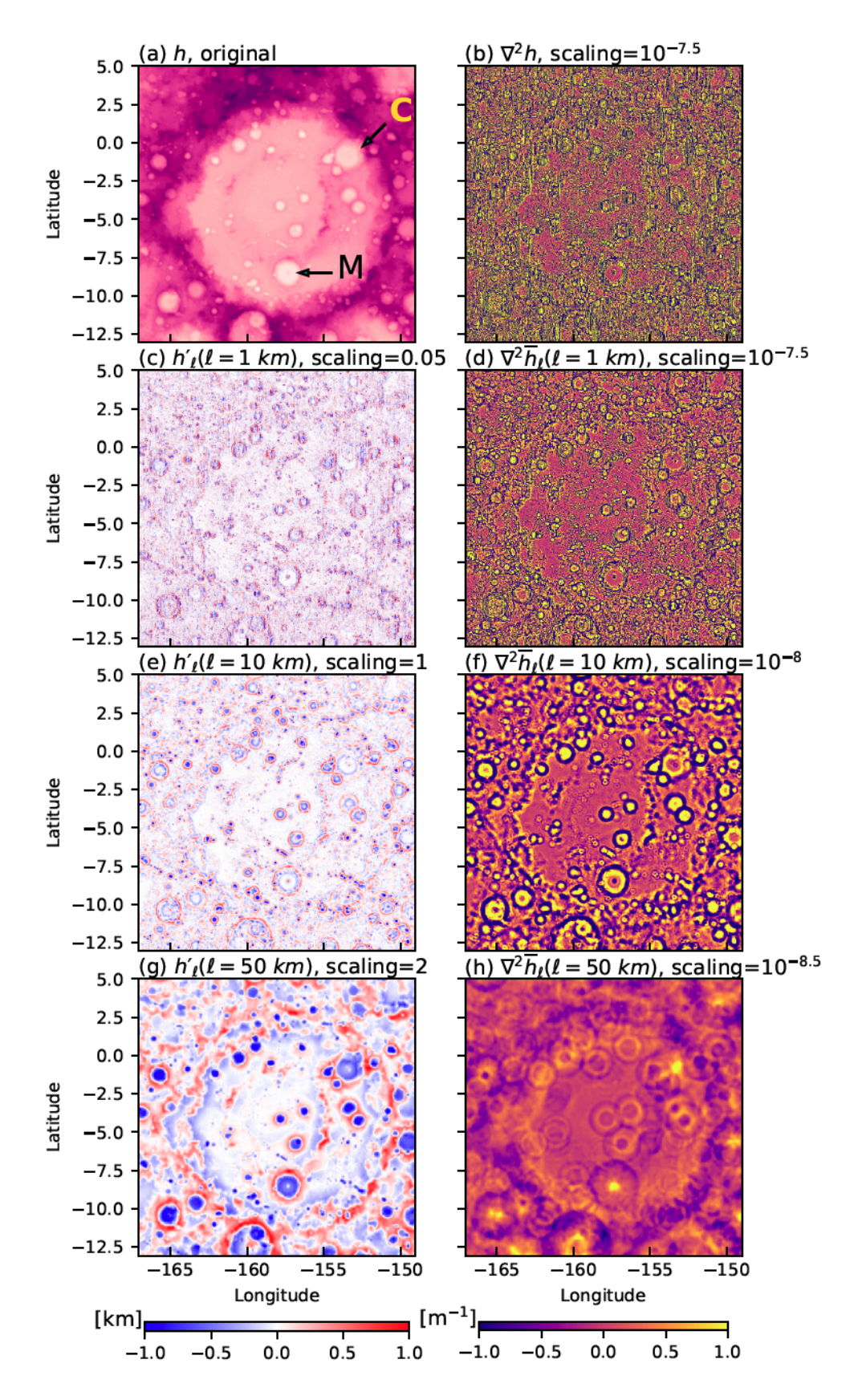


Figure 10. Korolev Basin (Left) the topography and fine elevation, h'_{ℓ} , and (right) the original curvature and coarse curvature, $\nabla^2 \overline{h}_{\ell}$, of the Korolev basin region at length-scales of (c,d) $\ell=1$ km, (e,f) $\ell=10$ km, and (g,h) $\ell=50$ km. In (a) [C] denotes Korolev C crater, and [M] the Korolev M crater. Each panel was normalized to share a common colorbar. The normalization factors are included in each panel label.

ible in $h'_{\ell=1km}$ and $h'_{\ell=5km}$. The walls of Cassini are narrow and outside the crater rim, there is a wide outer rampart. These features of narrow walls and wide outer rampart exist at all three length-scales. The nearby lunar mare has intruded into Montes Caucasus, especially in the southern parts. The evidence of intrusion exists in h'_{ℓ} at all three length-scales, implying that the intrusion parts and the mountains have different roughness characteristics. These maps of h'_{ℓ} help with identifying features that are not so obvious on the original topography map, such as impact ejecta, crater peak, and hilly ridge areas.

Rima Ariadaeus and Rima Hyginus In Figure 12, both Rima Ariadaeus (center right) and Rima Hyginus (center left) are most visible in $\nabla^2 \overline{h}_{\ell=1km}$ [12(b)]. Both rilles have clear edges marked by negative curvature. We can see Hyginus crater on top of Rima Hyginus, and Silberschlag crater joins Rima Ariadaeus by a small ridge. Rimae Triesnecker (bottom left corner) is also accented by the coarse curvature. Because it is shallower and narrower, Rimae Triesnecker has smaller curvature magnitudes than Rima Ariadaeus and Rima Hyginus. In $\nabla^2 \overline{h}_{\ell=1km}$, some irregularly shaped areas have higher curvature variations, indicating a higher surface roughness. In $\nabla^2 \overline{h}_{\ell=5km}$ [12(c)], both Rima Ariadaeus and Rima Hyginus are less detailed, and Rimae Triesnecker is barely visible. At $\ell=5$ km, the curvature starts to emphasize small craters. At $\ell=20$ km [12(d)], both Rima Ariadaeus and Rima Hyginus are smoothed out and hardly have any curvature. Rimae Triesnecker is completely omitted because $\ell=20$ km has exceedingly surpassed the length-scale of this feature. Small craters are also downplayed, and the large craters are highlighted. These maps of $\nabla^2 \overline{h}_{\ell}$ help with identifying small-scale and high-curvature features, such as rilles and small craters, from the original topography.

5 Conclusion

Coarse-graining is a simple yet powerful tool that can be integrated into various investigations on the topographic roughness properties of a spherical surface. The examples in this paper demonstrate that coarse-graining is especially useful when applying scale-dependent filters in the spherical coordinate, when a continuous wavenumber spectrum is desired, or when regional analysis is needed.

The coarse-graining method avoids projection distortions by utilizing the geodesic distance – it is not only scale-dependent but also maps the characteristics of both the polar region and the equator equally. The two metrics, fine elevation and coarse curvature, can be computed at any length-scale as long as the length-scale is shorter than the circumference of the sphere. The coarse-graining method is not sensitive to the resolution of input elevation data; thus, lower-resolution data can be used to map roughness at a large length-scale. Depending on the length-scale of interest, one can choose the appropriate resolution to conserve computational time. The implementation of the coarse-graining method is also highly parallelizable, making it computationally inexpensive. In addition, the coarse-graining method preserves the physical meaning of the original data. Lastly, the coarse-graining method is both deterministic and isotropic, ensuring robust mapping of roughness.

In this study, we have demonstrated that two surface variability metrics – fine elevation and coarse curvature – obtained through the coarse-graining method can help map lunar surface topography at a range of length-scales. Decomposing topography into different length-scales enables researchers to distinguish and characterize the fundamental processes in the creation of different geological units. By considering the fine elevation maps of the Korolev basin and Montes Caucasus regions, we demonstrate how different geological features can have distinct roughness characteristics across scales. The second metric used in this paper is the coarse curvature $\nabla^2 \overline{h}_{\ell}$, which computes the Laplacian of the coarse elevation. $\nabla^2 \overline{h}_{\ell}$ emphasizes small-scale changes in the coarse elevation and is a decent tool to highlight any sudden change in the surface topography. Plots

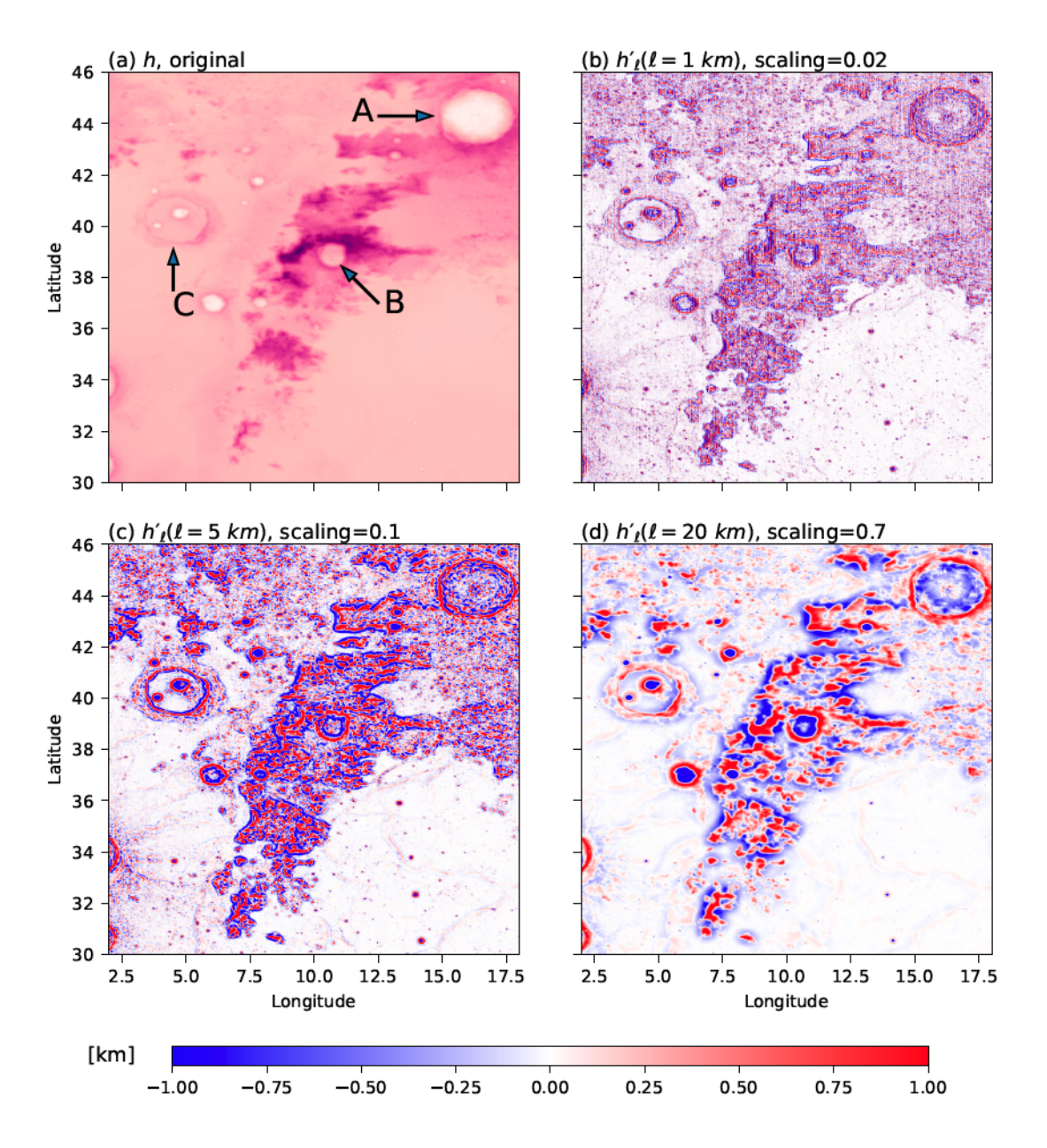


Figure 11. Montes Caucasus (a) Unfiltered topography of the Montes Caucasus region and fine elevation, h'_{ℓ} , at length-scales of (b) $\ell=1$ km, (c) $\ell=5$ km, and (d) $\ell=20$ km. In (a), [A] denotes the Eudoxus crater, [B] the Calippus crater, and [C] the Cassini crater.

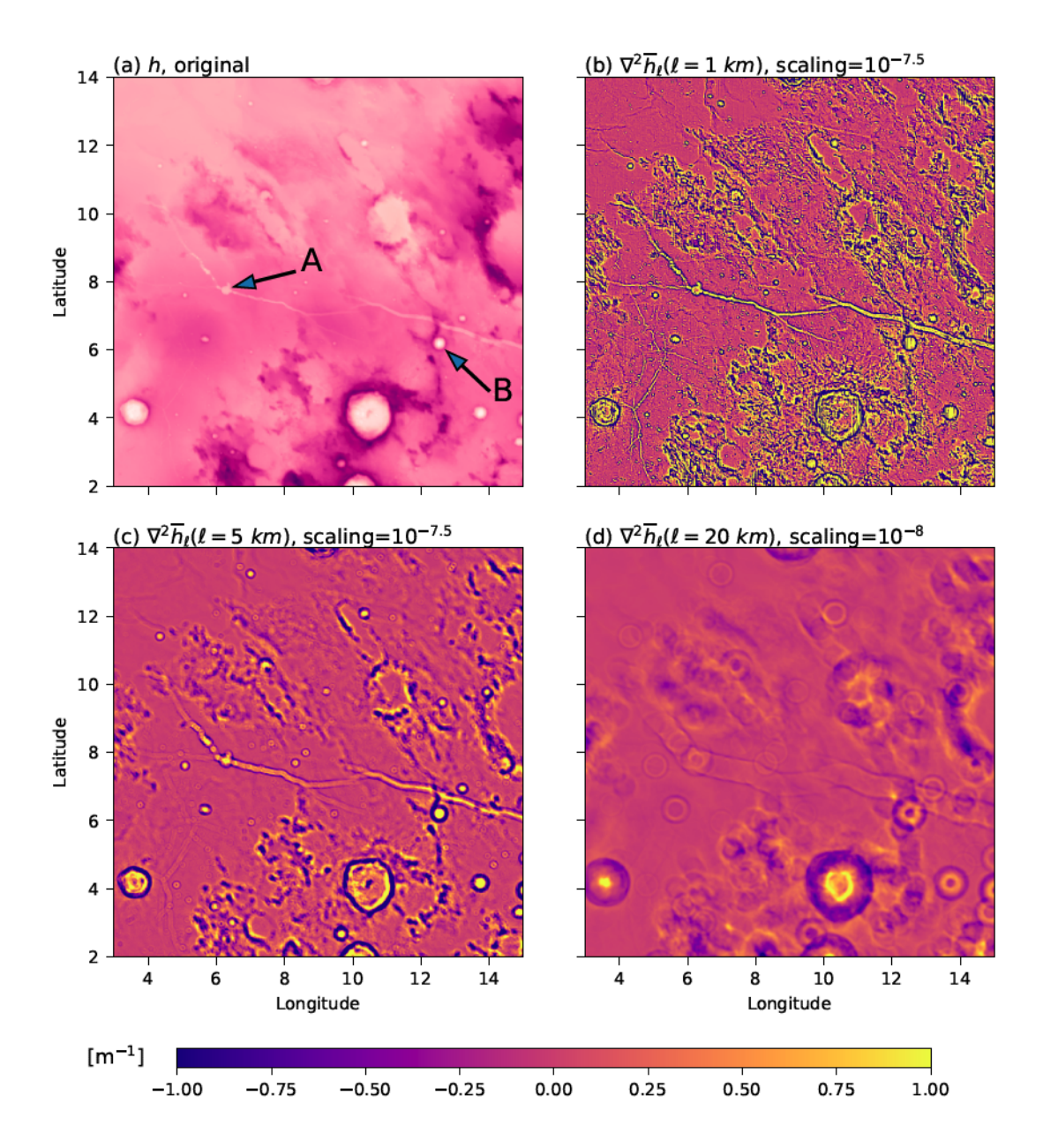


Figure 12. Rimae The (a) original curvature and (b-d) coarse curvature, $\nabla^2 \overline{h}_{\ell}$, of the region including Rima Hyginus and Rima Ariadaeus, at length-scales of (b) $\ell=1$ km, (c) $\ell=5$ km, and (d) $\ell=20$ km. In the topography: [A] Hyginus crater, and [B] Silberschlag crater.

of $\nabla^2 \overline{h}_{\ell}$ near the Korolev basin as well as Rima Hyginus and Rima Ariadaeus demonstrate how rilles, crater rims, and crater peaks are highlighted in $\nabla^2 \overline{h}_{\ell}$. Lastly, while it is possible to also create a spectrum for the coarse curvature, we exclude it in this study, due to the complexity of the Laplacian.

Since it is possible to obtain the fine elevation at any length-scale within the planetary diameter, we can obtain a continuous filtering spectrum with respect to the length-scale. The slope of the log-log filtering spectrum can help identify scale breaks — length-scales corresponding to shifts in roughness characteristics. In this study, we have identified 100 km, 300 km, 1000 km, and 4000 km as the important length-scales among lunar surface features. Rosenburg et al. (2011) identify a scale break near 1 km when comparing lunar surface roughness of length-scales shorter than 3 km. A scale break near 30 km was identified by Yokota et al. (2014) using both synthetic and observational data. This finding matches with the 30 km length-scaled we noticed. Three scale break intervals, 330–659 m, 1.3–21.1 km, and 42.2–168.8 km, are also suggested by Lemelin et al. (2020) using Hölder exponents. The 42.2–168.8 km scale break ranges coincide with the 100 km scale break we discovered using the coarse-graining method. We also identified 1.5 km to be an interesting length-scale; however, more roughness measurements with length-scales smaller than 1 km are needed to assert 1.5 km as a scale break.

Data Availability Statement

The data required to reproduce the results presented here will be made available through a Zenodo archive upon acceptance. The source code for the coarse-graining software FlowSieve (Storer & Aluie, 2023) has been archived on Zenodo https://doi.org/10.5281/zenodo.7818192. More information on the coarse-graining software, including installation and tutorials, can be found at https://flowsieve.readthedocs.io/en/latest/index.html.

A temporary shared folder containing all relevant data and scripts is available for the review process, and can be accessed at https://rochester.box.com/s/nnlzxksa9zylwtnbgh48n45ecetjfxh7. Upon acceptance, these documents will be made available through a public archive.

Acknowledgments

618

619

620

622

623

624

627

628

629

631

632

635

636

638

641

642

643

647

658

659

660

663

664

665

We thank two reviewers for their careful reading of our paper and their constructive criticism. We acknowledge helpful discussions with Miki Nakajima, Tolulope Olugboji, Yaocheng Tian, Mehrnoush Kharghani, Abdus Samad, and Dina Soltani Tehrani. We acknowledge partial support from US NSF grant OCE-2123496 and NASA grant 80NSSC18K0772.

HA was also supported by US DOE grants DE-SC0020229, DE-SC0014318, DE-SC0019329, US NSF grant PHY-2020249, PHY-2206380, and US NNSA grants DE-NA0003856, DE-NA0003914, DE-NA0004134. Computing time was provided by NERSC under Contract No. DE-AC02-05CH11231, and the Texas Advanced Computing Center (TACC) at The University of Texas at Austin, under ACCESS allocation grant EES220052.

References

Aluie, H. (2017). Coarse-grained incompressible magnetohydrodynamics: analyzing the turbulent cascades. New Journal of Physics, 19, 025008.

Aluie, H. (2019). Convolutions on the sphere: commutation with differential operators. International Journal on Geomathematics, 10(9). doi: https://doi.org/10.1007/s13137-019-0123-9

Aluie, H., Hecht, M., & Vallis, G. K. (2018). Mapping the energy cascade in the north atlantic ocean: The coarse-graining approach. *Journal of Physical Oceanography*, 48(2), 225 - 244. doi: 10.1175/JPO-D-17-0100.1

Aluie, H., Rai, S., Yin, H., Lees, A., Zhao, D., Griffies, S. M., ... Shang, J. K.

(2022). Effective drift velocity from turbulent transport by vorticity. *Physical Review Fluids*, 7(10), 104601.

- Anderson, R. S., & Anderson, S. P. (2010). Geomorphology: the mechanics and chemistry of landscapes. Cambridge University Press.
- Buzzicotti, M., Storer, B. A., Khatri, H., Griffies, S. M., & Aluie, H. (2023). Spatiotemporal coarse-graining decomposition of the global ocean geostrophic kinetic energy. *Journal of Advances in Modeling Earth Systems*, 15(6), e2023MS003693. doi: https://doi.org/10.1029/2023MS003693
- Cai, Y., & Fa, W. (2020). Meter-scale topographic roughness of the moon: The effect of small impact craters. *Journal of Geophysical Research: Planets*, 125(8), e2020JE006429. doi: https://doi.org/10.1029/2020JE006429
- Cao, W., Cai, Z., & Tang, Z. (2015). Lunar surface roughness based on multiscale morphological method. *Planetary and Space Science*, 108, 13-23. doi: https://doi.org/10.1016/j.pss.2014.09.009
- Deliège, A., Kleyntssens, T., & Nicolay, S. (2017). Mars topography investigated through the wavelet leaders method: A multidimensional study of its fractal structure. Planetary and Space Science, 136, 46-58. doi: https://doi.org/10.1016/j.pss.2016.12.008
- Doane, T. H., Edmonds, D., Yanites, B. J., & Lewis, Q. (2021). Topographic roughness on forested hillslopes: A theoretical approach for quantifying hillslope sediment flux from tree throw. Geophysical Research Letters, 48 (20), e2021GL094987. doi: https://doi.org/10.1029/2021GL094987
- Doane, T. H., Yanites, B. J., Edmonds, D. A., & Novick, K. A. (2023). Hill-slope roughness reveals forest sensitivity to extreme winds. *Proceedings of the National Academy of Sciences*, 120(3), e2212105120. doi: 10.1073/pnas.2212105120
- Evans, L. C. (2010). Partial Differential Equations. Amer Mathematical Society.
 - Eyink, G. L. (2005). Locality of turbulent cascades. *Physica D: Nonlinear Phenomena*, 207(1-2), 91–116.
 - Garrick-Bethell, I., Nimmo, F., & Wieczorek, M. A. (2010). Structure and formation of the lunar farside highlands. Science, 330 (6006), 949-951. doi: 10.1126/science.1193424
 - Grieve, S. W., Mudd, S. M., Milodowski, D. T., Clubb, F. J., & Furbish, D. J. (2016). How does grid-resolution modulate the topographic expression of geomorphic processes? *Earth Surface Dynamics*, 4(3), 627–653.
 - Jaffard, S. (2004). Wavelet techniques in multifractal analysis. Proceedings of Symposia in Pure Mathematics, 72, 91-152. doi: https://doi.org/10.1090/pspum/072.2
 - Khatri, H., Griffies, S. M., Storer, B. A., Buzzicotti, M., Aluie, H., Sonnewald, M., ... Shao, A. (2024). A scale-dependent analysis of the barotropic vorticity budget in a global ocean simulation. *Journal of Advances in Modeling Earth* Systems, 16(6), e2023MS003813.
 - Krantz, S. G. (2019). A panorama of harmonic analysis (Vol. 27). American Mathematical Society.
 - Kreslavsky, M. A. (2023). Detrended topography of the moon [Dataset]. Zenodo. Retrieved from https://doi.org/10.5281/zenodo.10340214 doi: 10.5281/zenodo.10340213
- Kreslavsky, M. A., Head, J. W., Neumann, G. A., Rosenburg, M. A., Aharonson, O., Smith, D. E., & Zuber, M. T. (2013). Lunar topographic roughness maps from lunar orbiter laser altimeter (lola) data: Scale dependence and correlation with geologic features and units. *Icarus*, 226(1), 52-66. doi: https://doi.org/10.1016/j.icarus.2013.04.027
- Kreslavsky, M. A., Head, J. W., Neumann, G. A., Zuber, M. T., & Smith, D. E. (2017). Low-amplitude topographic features and textures on the moon:

Initial results from detrended lunar orbiter laser altimeter (lola) topography. *Icarus*, 283, 138-145. (Lunar Reconnaissance Orbiter - Part II) doi: https://doi.org/10.1016/j.icarus.2016.07.017

721

722

723

724

725

726

727

728

731

732

733

734

737

738

740

741

743

744

745

746

749

750

751

752

753

755

756

757

758

761

762

763

764

765

767

768

770

771

773

774

775

- Kreslavsky, M. A., & Head III, J. W. (2000). Kilometer-scale roughness of mars: Results from mola data analysis. *Journal of Geophysical Research: Planets*, 105(E11), 26695-26711. doi: https://doi.org/10.1029/2000JE001259
- Lemelin, M., Daly, M., & Deliège, A. (2020). Analysis of the topographic roughness of the moon using the wavelet leaders method and the lunar digital elevation model from the lunar orbiter laser altimeter and selene terrain camera. Journal of Geophysical Research: Planets, 125(1), e2019JE006105. doi: https://doi.org/10.1029/2019JE006105
- Matheron, G. (1963). Principles of geostatistics. *Economic Geology*, 58(8), 1246-1266. doi: 10.2113/gsecongeo.58.8.1246
- Nelson, D. M., Koeber, S. D., Daud, K., Robinson, M. S., Watters, T. R., Banks, M. E., & Williams, N. R. (2014). Mapping lunar maria extents and lobate scarps using lroc image products (Vol. 45) [Dataset]. Retrieved from https://wms.lroc.asu.edu/lroc/view_rdr/SHAPEFILE_LROC_GLOBAL_MARE
- Neumann, G. (2010). Resampled (binned), interpolated altimetry data products from the 2009 lunar reconnaissance orbiter mission. [Dataset]. NASA Planetary Data System. Retrieved from https://pds-geosciences.wustl.edu/missions/lro/lola.htm doi: 10.17189/1520642
- Pardo-Igúzquiza, E., & Dowd, P. (2022). Fractal analysis of the martian landscape: A study of kilometre-scale topographic roughness. *Icarus*, 372, 114727. doi: https://doi.org/10.1016/j.icarus.2021.114727
- Rai, S., Hecht, M., Maltrud, M., & Aluie, H. (2021). Scale of oceanic eddy killing by wind from global satellite observations. Science Advances, 7(28), eabf4920.
- Rivera, M., Aluie, H., & Ecke, R. E. (2014). The direct enstrophy cascade of twodimensional soap film flows. Physics of Fluids, 26(5).
- Robbins, S. J. (2019). A new global database of lunar impact craters > 1-2 km:

 1. crater locations and sizes, comparisons with published databases, and global analysis [Dataset]. Journal of Geophysical Research: Planets. Retrieved from https://agupubs.onlinelibrary.wiley.com/doi/abs/10.1029/2018JE005592 doi: https://doi.org/10.1029/2018JE005592
- Robbins, S. J., Riggs, J. D., Weaver, B. P., Bierhaus, E. B., Chapman, C. R., Kirchoff, M. R., . . . Gaddis, L. R. (2018). Revised recommended methods for analyzing crater size-frequency distributions. *Meteoritics and Planetary Science*, 53(4), 891–931. doi: 10.1111/maps.12990
- Rosenburg, M. A., Aharonson, O., Head, J. W., Kreslavsky, M. A., Mazarico, E., Neumann, G. A., . . . Zuber, M. T. (2011). Global surface slopes and roughness of the moon from the lunar orbiter laser altimeter. *Journal of Geophysical Research: Planets*, 116(E2). doi: https://doi.org/10.1029/2010JE003716
- Sadek, M., & Aluie, H. (2018). Extracting the spectrum of a flow by spatial filtering. Phys. Rev. Fluids, 3, 124610. doi: 10.1103/PhysRevFluids.3.124610
- Shepard, M. K., Campbell, B. A., Bulmer, M. H., Farr, T. G., Gaddis, L. R., & Plaut, J. J. (2001). The roughness of natural terrain: A planetary and remote sensing perspective. *Journal of Geophysical Research: Planets*, 106 (E12), 32777-32795. doi: https://doi.org/10.1029/2000JE001429
- Smith, D. E., Zuber, M. T., Jackson, G. B., Cavanaugh, J. F., Neumann, G. A., Riris, H., ... Zagwodzki, T. W. (2010). The lunar orbiter laser altimeter investigation on the lunar reconnaissance orbiter mission. Space Science Reviews, 150(1), 209-241. doi: 10.1007/s11214-009-9512-y
- Smith, M. W. (2014). Roughness in the earth sciences. *Earth-Science Reviews*, 136, 202-225. doi: https://doi.org/10.1016/j.earscirev.2014.05.016
- Sogge, C. D. (2017). Fourier integrals in classical analysis (Vol. 210). Cambridge University Press.

Storer, B. A., & Aluie, H. (2023). Flowsieve: A coarse-graining utility for geophysical flows on the sphere [Software]. The Journal of Open Source Software. Retrieved from https://flowsieve.readthedocs.io/en/latest/index.html doi: 10.21105/joss.04277

776

777

778

780

781

782

783

784

785

788

789

790

791

792

793

796

797

798

- Storer, B. A., Buzzicotti, M., Khatri, H., Griffies, S. M., & Aluie, H. (2022). Global energy spectrum of the general oceanic circulation. *Nature Communications*, 13(1), 5314. doi: 10.1038/s41467-022-33031-3
- Storer, B. A., Buzzicotti, M., Khatri, H., Griffies, S. M., & Aluie, H. (2023). Global cascade of kinetic energy in the ocean and the atmospheric imprint. Science Advances, 9(51), eadi7420.
- Strichartz, R. S. (2003). A guide to distribution theory and fourier transforms. World Scientific Publishing Company.
- Wieczorek, M. (2024). Spherical harmonic models of the shape of the moon (principal axis coordinate system) [lola] (1.0.1) [Dataset]. Zenodo. Retrieved from https://doi.org/10.5281/zenodo.10820750 doi: 10.5281/zenodo.10820750
- Yokota, Y., Gwinner, K., Oberst, J., Haruyama, J., Matsunaga, T., Morota, T., . . . Demura, H. (2014). Variation of the lunar highland surface roughness at baseline 0.15–100 km and the relationship to relative age. Geophysical Research Letters, 41(5), 1444-1451. doi: https://doi.org/10.1002/2013GL059091
- Zhao, D., & Aluie, H. (2023). Measuring scale-dependent shape anisotropy by coarse-graining: Application to inhomogeneous rayleigh-taylor turbulence. *Physical Review Fluids*, 8(11), 114601.

Supporting Information Appendix (SI)

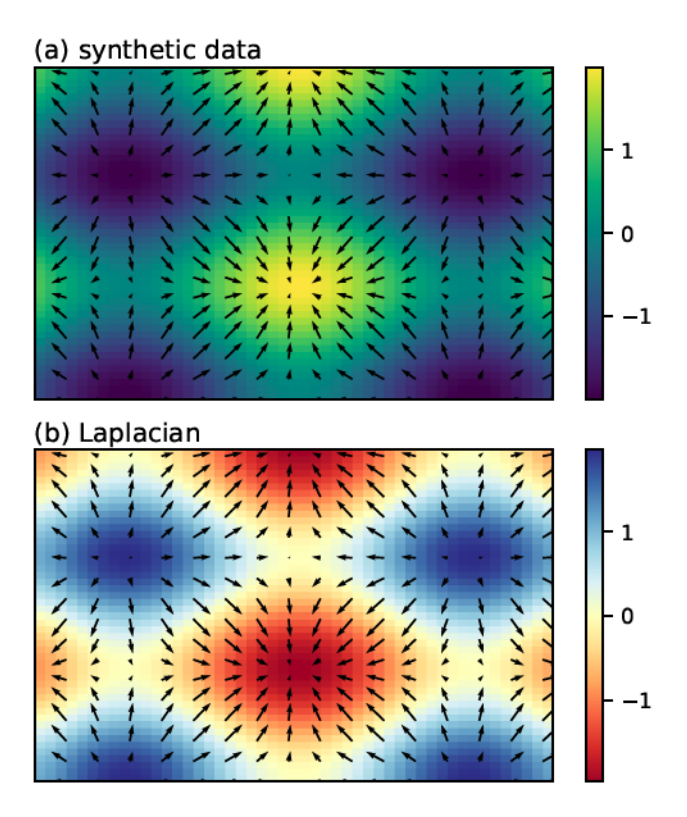


Figure S1. (a) shows the synthetic data that has both concave and convex shapes. The gradient also points to the direction of the greatest ascent; therefore, we see sources and sinks corresponding to the synthetic data curving down or up. (b) shows the divergence of the gradient, which is the Laplacian, that measures how much the scalar function locally behaves like a sink or source. Having a negative Laplacian means that this point is higher than its neighboring points, and having a positive Laplacian means that this point is lower than its neighboring points. As a result, the Laplacian will be positive near a minimum and negative near a maximum. The sign and magnitude together allow the coarse curvature to preserve the physical meaning of the surface.

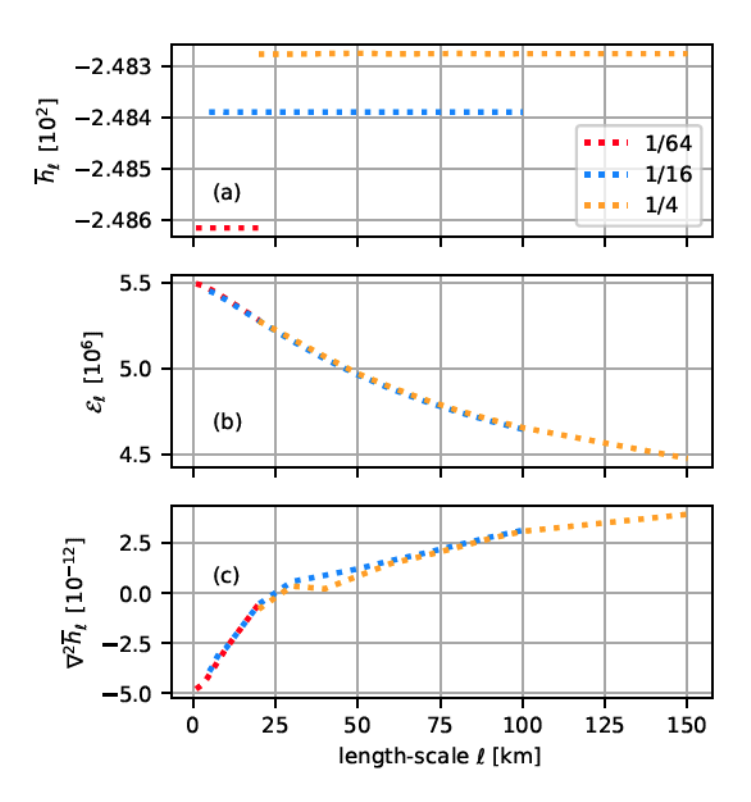


Figure S2. Compare (a) \overline{h}_{ℓ} , (b) \mathcal{E}_{ℓ} , and (c) $\nabla^2 \overline{h}_{\ell}$ of the entire Moon surface in the 1–100 km length-scales range using elevation data with resolutions of 64 pixels per degree, 16 pixels per degree, and 4 pixels per degree. The overlapping curves indicate a convergence across data resolution. The slight differences are due to numerical errors and the difference across elevation models.